Supplementary Information

2D spin crossover coordination polymers based on 1,1,2,2-tetra(pyridin-4-yl)ethene ligand

Meng-Ling Wu,[a] Yan-Cong Chen[a], Ze-Yu Ruan[a], Zhao-Ping Ni,[a] Si-Guo Wu[a]* and Ming-Liang Tong[a]*

[a]Key Laboratory of Bioinorganic and Synthetic Chemistry of Ministry of Education, School of Chemistry, IGCME, GBRCE for Functional Molecular Engineering, Sun Yat-Sen University, Guangzhou 510275 (P. R. China)

Table of Contents:

Crystal Data and structure

Table S1. Crystallographic data and structural refinements for **1**.

Temperature	120 K	300 K
Formula	$C_{29}H_{39}B_2FeN_7O_4$	$C_{29}H_{39}B_2FeN_7O_4$
Formula weight	627.14	627.14
Crystal system	Tetragonal	Tetragonal
Space group	*I*422	*I*422
a / Å	9.5472(3)	9.8102(6)
b / Å	9.5472(3)	9.8102(6)
c / Å	16.7921(10)	17.649(3)
α / °	90	90
β / °	90	90
γ / °	90	90
V / Å^3	1530.58(13)	1698.5(4)
Z	2	2
$\rho_{calcd.}$ / g/cm^{-3}	1.361	1.226
μ / mm^{-1}	0.54	0.49
F(000)	660	660
Crystal size / mm^3	0.15 × 0.14 × 0.03	0.20 × 0.16 × 0.03
Reflections collected	5330	6706
Independent reflections	796	891
GOF on F^2	1.179	1.107
R_1 [$I \geq 2\sigma(I)$][a]	R_1 = 0.0289, wR_2 = 0.0696	R_1 = 0.0549, wR_2 = 0.1346
wR_2 (all data)	R_1 = 0.0308, wR_2 = 0.0703	R_1 = 0.0598, wR_2 = 0.1369
Largest diff. peak/hole / eÅ^{-3}	0.30/−0.21	0.33/−0.52
CCDC No.	2326668	2326669

[a] $R_1 = \sum||F_o| - |F_c||/\sum|F_o|$. $wR_2 = [\sum w(F_o^2 - F_c^2)^2/\sum w(F_o^2)^2]^{1/2}$

Table S2. Crystallographic data and structural refinements for **2**.

Temperature	120 K	250 K
Formula	$C_{27.5}H_{29.5}FeN_{6.5}Se_2O_{3.5}$	$C_{27.5}H_{29.5}FeN_{6.5}Se_2O_{3.5}$
Formula weight	720.84	720.84
Crystal system	Tetragonal	Tetragonal
Space group	*I*422	*I*422
a / Å	9.5479(5)	9.8316(4)
b / Å	9.5479(5)	9.8316(4)
c / Å	16.7363(19)	17.3768 (18)
α / °	90	90
β / °	90	90
γ / °	90	90
V / Å^3	1525.7(2)	1679.6(2)
Z	2	2
$\rho_{calcd.}$ / g/cm^{-3}	1.569	1.425
μ / mm^{-1}	2.92	2.65
F(000)	724	724
Crystal size / mm^3	0.16 × 0.09 × 0.04	0.19 × 0.09 × 0.02
Reflections collected	7965	5361
Independent reflections	958	971
GOF on F^2	1.114	1.088
Final *R* indexes [$I \geq 2\sigma(I)$][a]	R_1 = 0.0685, wR_2 = 0.1904	R_1 = 0.0829, wR_2 = 0.2373
Final *R* indexes [all data]	R_1 = 0.0825, wR_2 = 0.1996	R_1 = 0.0978, wR_2 = 0.2493
Largest diff. peak/hole / eÅ^{-3}	1.40/−0.63	1.09/−1.08
CCDC No.	2326670	2326671

[a] $R_1 = \sum||F_o| - |F_c||/\sum|F_o|$. $wR_2 = [\sum w(F_o^2 - F_c^2)^2/\sum w(F_o^2)^2]^{1/2}$

Table S3. Crystallographic data and structural refinements for **3**.

Temperature	120 K	250 K
Formula	$C_{27.5}H_{29.5}FeN_{6.5}S_2O_{3.5}$	$C_{27.5}H_{29.5}FeN_{6.5}S_2O_{3.5}$
Formula weight	627.04	627.04
Crystal system	Tetragonal	Tetragonal
Space group	*I*422	*I*422
a / Å	9.54260(10)	9.8267(12)
b / Å	9.54260(10)	9.8267(12)
c / Å	16.2834(7)	16.767(4)
α / °	90	90
β / °	90	90
γ / °	90	90
V / Å^3	1482.79(7)	1619.1(6)
Z	2	2
$\rho_{calcd.}$ / g/cm^{-3}	1.404	1.286
μ / mm^{-1}	0.69	0.63
F(000)	652	652
Crystal size / mm^3	0.10 × 0.06 × 0.04	0.10 × 0.06 × 0.04
Reflections collected	1800	6100
Independent reflections	924	939
GOF on F^2	1.015	1.120
Final *R* indexes [$I \geq 2\sigma(I)$][a]	R_1 = 0.0549, wR_2 = 0.1329	R_1 = 0.0454, wR_2 = 0.1196
Final *R* indexes [all data]	R_1 = 0.0683, wR_2 = 0.1389	R_1 = 0.0515, wR_2 = 0.1210
Largest diff. peak/hole / eÅ^{-3}	0.73/−0.32	0.46/−0.44
CCDC No.	2326672	2326673

[a] $R_1 = \sum||F_o| - |F_c||/\sum|F_o|$. $wR_2 = [\sum w(F_o^2 - F_c^2)^2/\sum w(F_o^2)^2]^{1/2}$

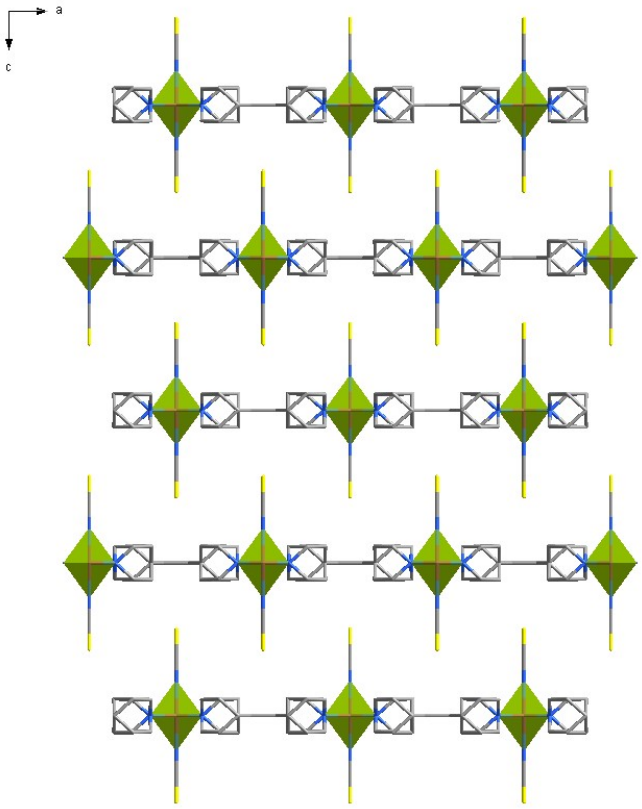

Figure S1. The view of 2D layers packing of **1** along the *c*-axis.

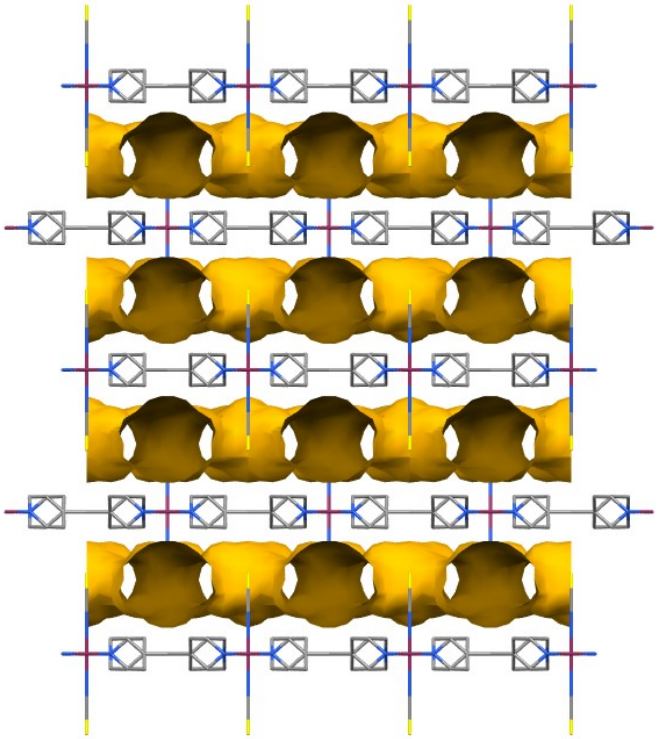

Figure S2. The interlayered voids of **1**. The solvent molecules and hydrogen atoms are omitted for clarity. The volume of voids accounts for 27.6 % of unit cell volume.

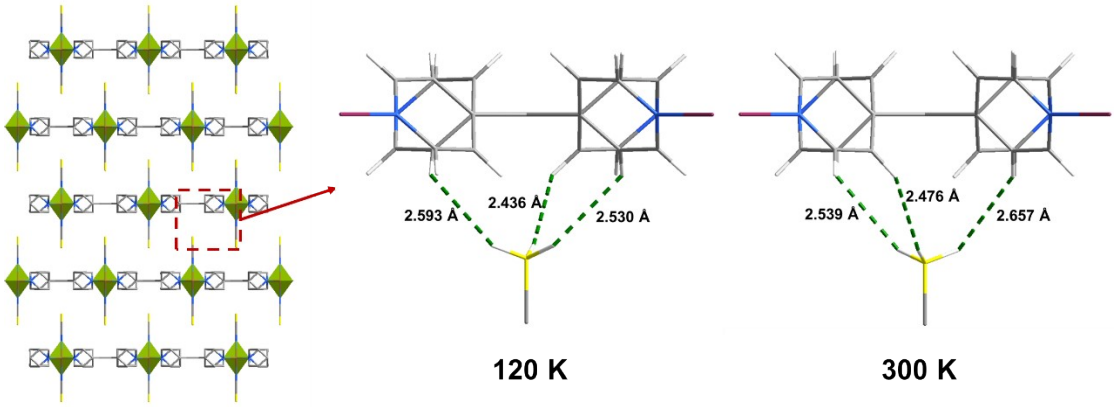

Figure S3. The view of 2D layers packing of **1** along the *c*-axis (left). The solvent molecules and hydrogen atoms are omitted for clarity. The potential dihydrogen interactions between layers (right).

PXRD

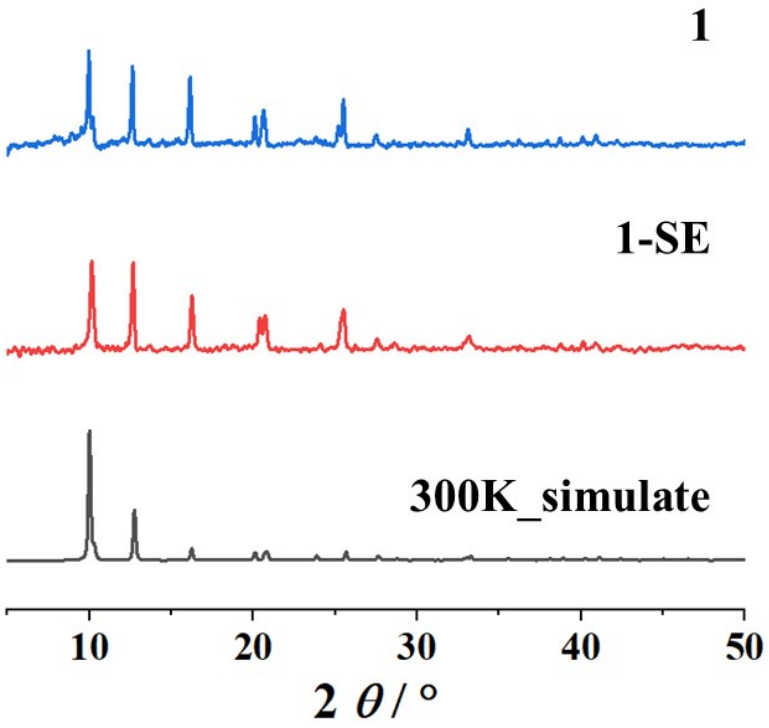

Figure S4. The experimental and simulated powder X-ray diffraction (PXRD) patterns for **1** and **1-SE**.

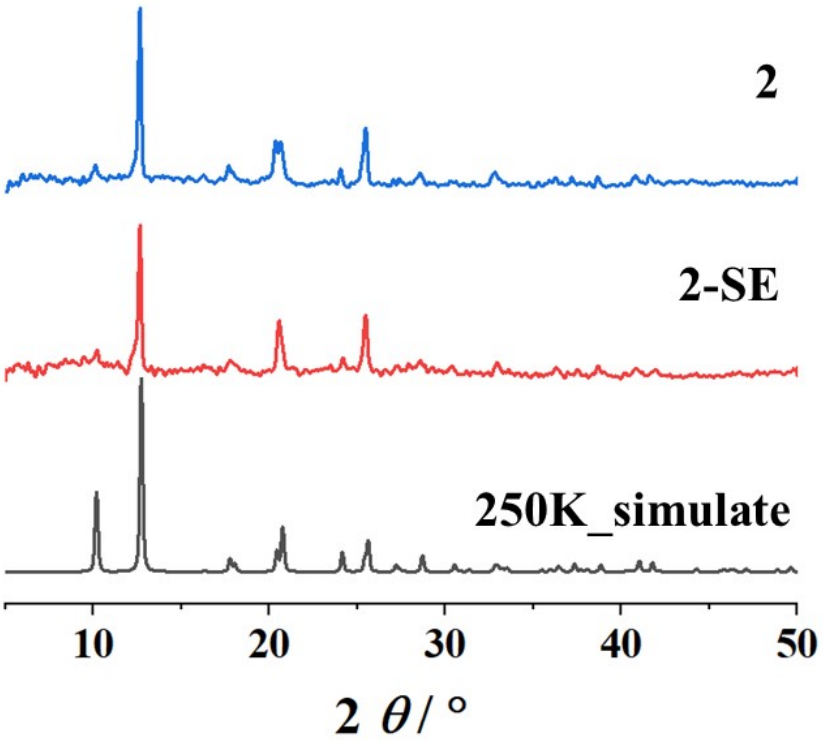

Figure S5. The experimental and simulated powder X-ray diffraction (PXRD) patterns for **2** and **2-SE**.

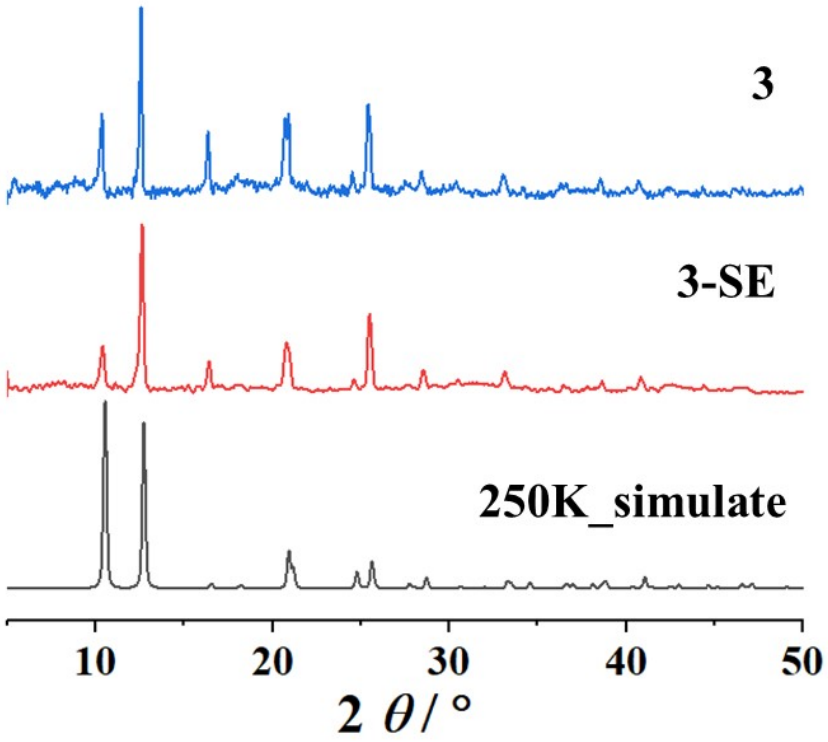

Figure S6. The experimental and simulated powder X-ray diffraction (PXRD) patterns for **3** and **3-SE**.

TG

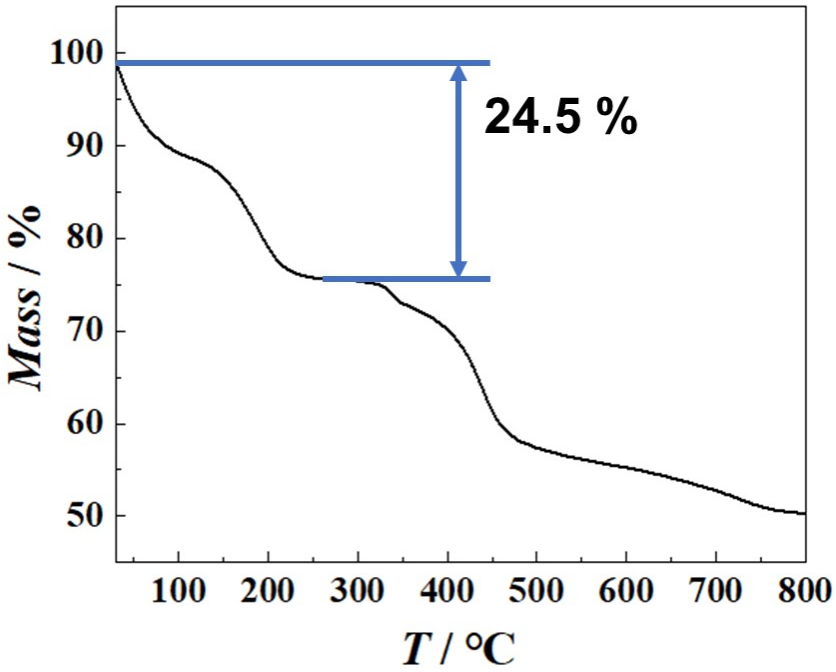

Figure S7. Thermogravimetric analysis (TGA) curve of **1**. The weight loss of ca. 24.5% is close to the theoretical value of 24.75% corresponding to the escape of 1 H_2O, 2 MeOH and 1 DMF molecules.

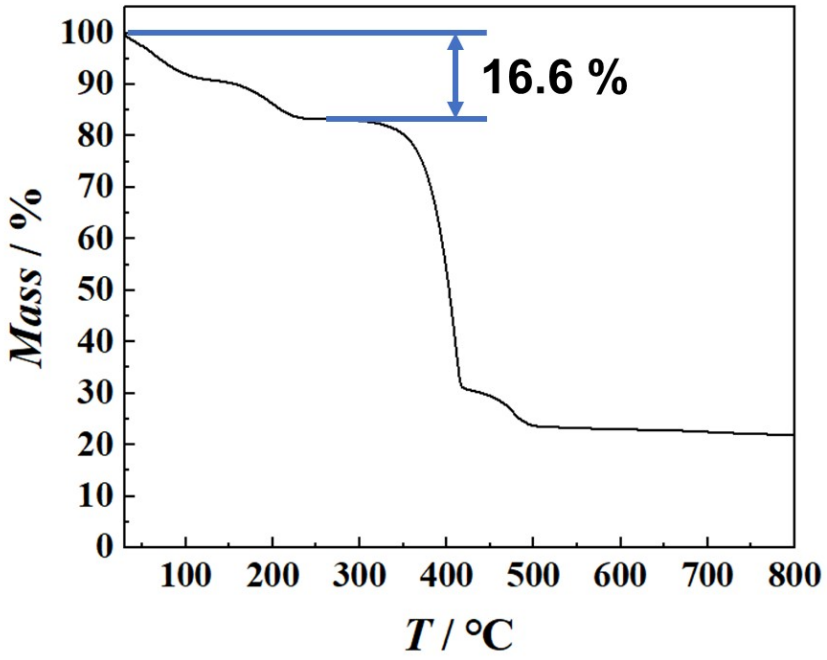

Figure S8. Thermogravimetric analysis (TGA) curve of **2**. The weight loss of ca. 16.6% is close to the theoretical value of 16.46% corresponding to the escape of 1 H_2O, 2 MeOH and 0.5 DMF molecules.

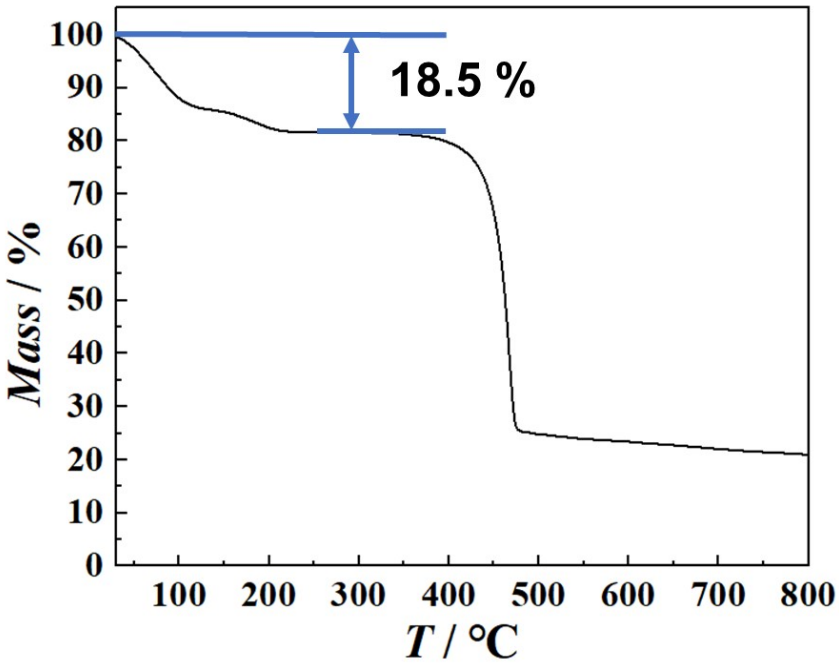

Figure S9. Thermogravimetric analysis (TGA) curve of **3**. The weight loss of ca. 18.5% is close to the theoretical value of 18.92% corresponding to the escape of 1 H_2O, 2 MeOH and 0.5 DMF molecules.

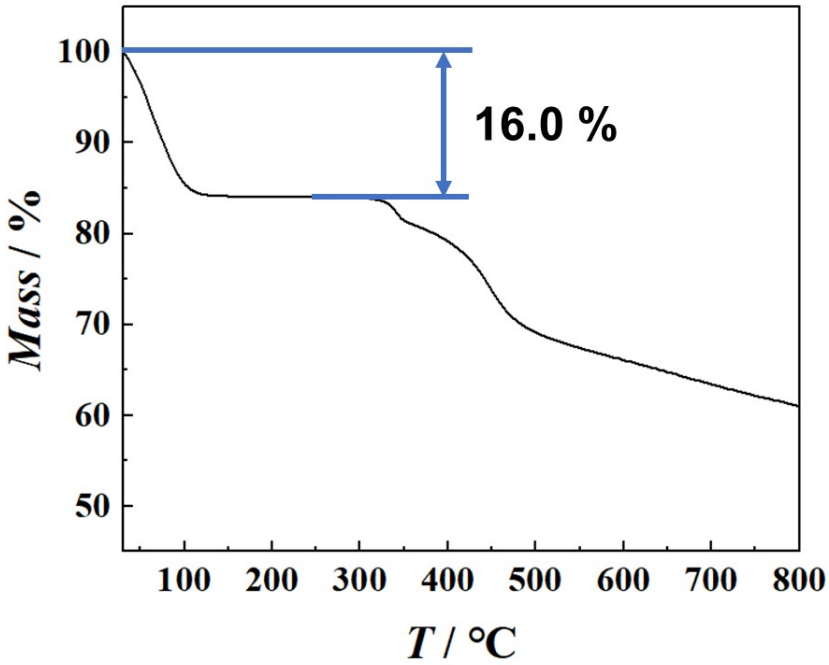

Figure S10. Thermogravimetric analysis (TGA) curve of **1-SE**. The weight loss of ca. 16.0% less than the theoretical value of 19.48% (corresponding to 1 H_2O and 3 MeOH) is due to the partial loss of methanol during the sample preparation.

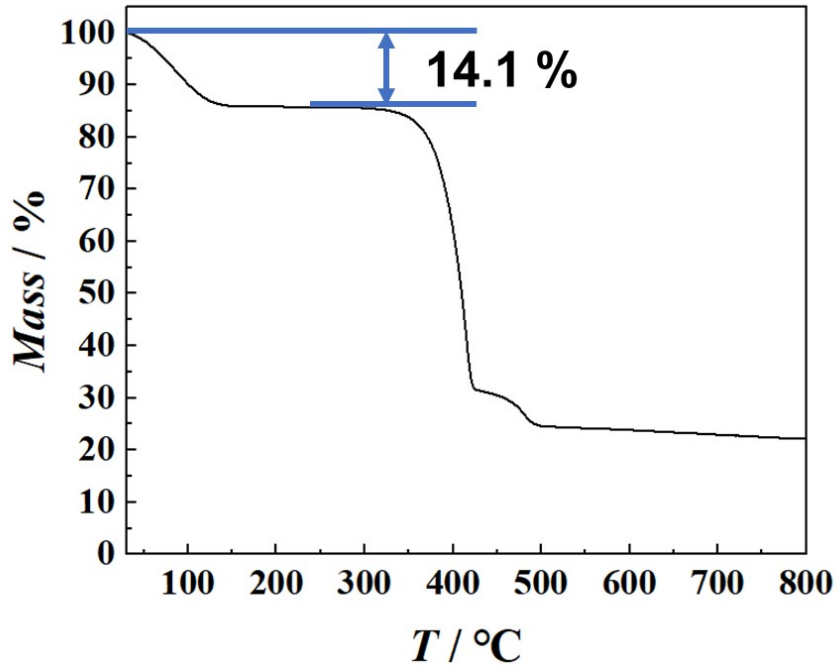

Figure S11. Thermogravimetric analysis (TGA) curve of **2-SE**. The weight loss of ca. 14.1% less than the theoretical value of 15.93% (corresponding to 1 H_2O and 3 MeOH) is due to the partial loss of methanol during the sample preparation.

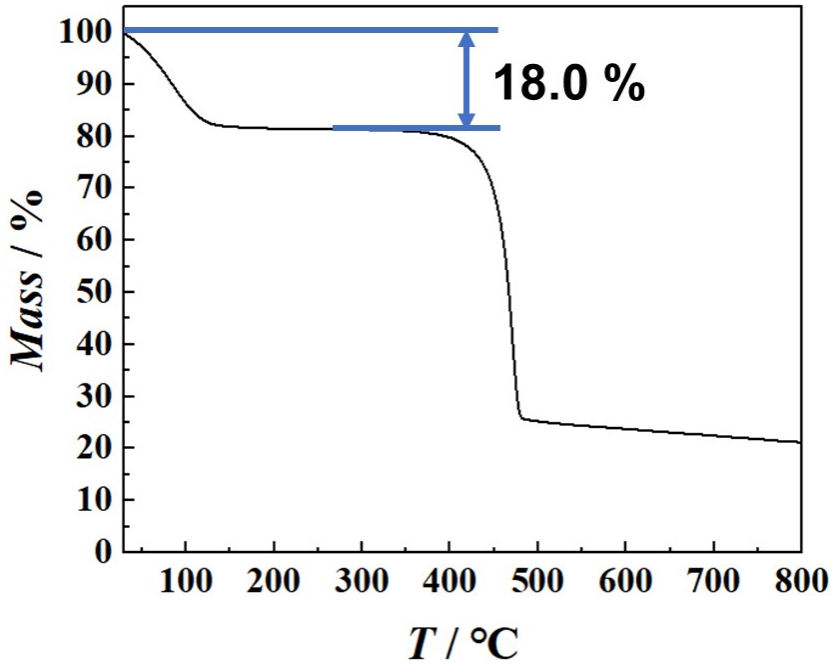

Figure S12. Thermogravimetric analysis (TGA) curve of **3-SE**. The weight loss of ca. 18.0% is close to the theoretical value of 18.33% corresponding to the escape of 1 H_2O and 3 MeOH.

UV-Vis

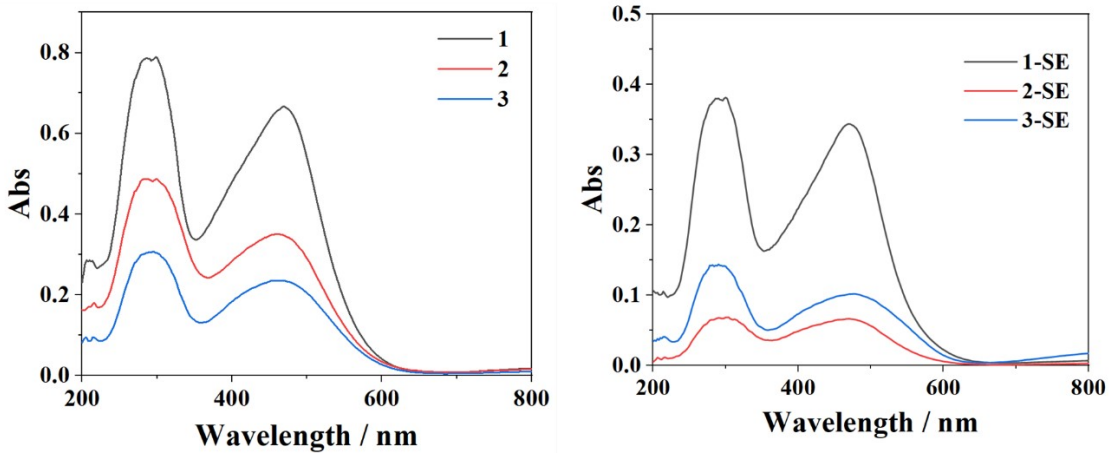

Figure S13. The UV-Vis spectra of **1**–**3** and the solvent-exchanged phases.

Magnetic Characterization

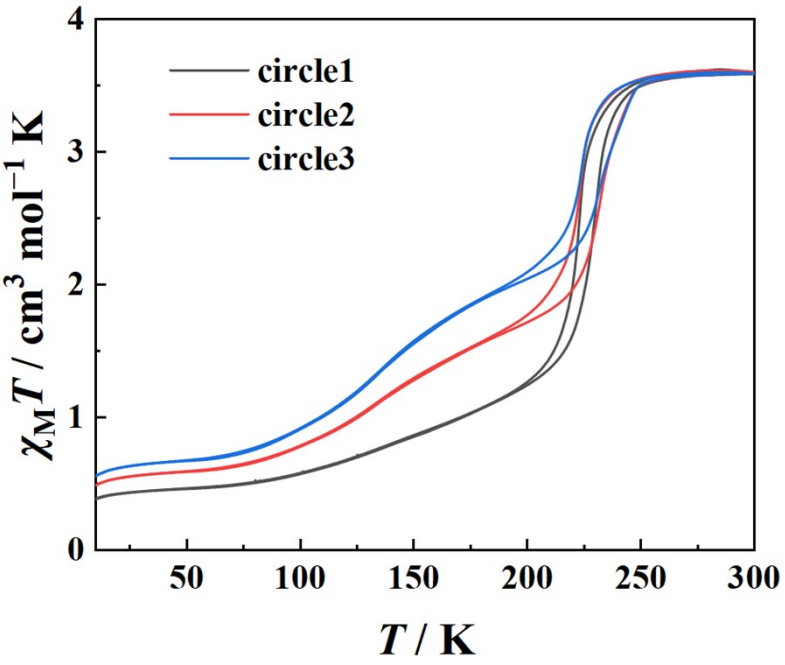

Figure S14. Variable-temperature magnetic susceptibilities of **1**.

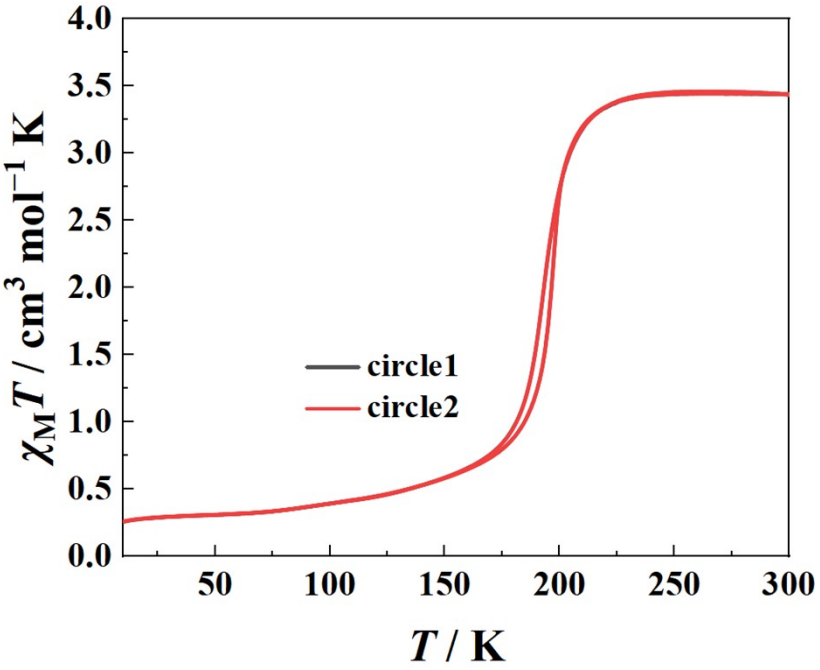

Figure S15. Variable-temperature magnetic susceptibilities of **2**.

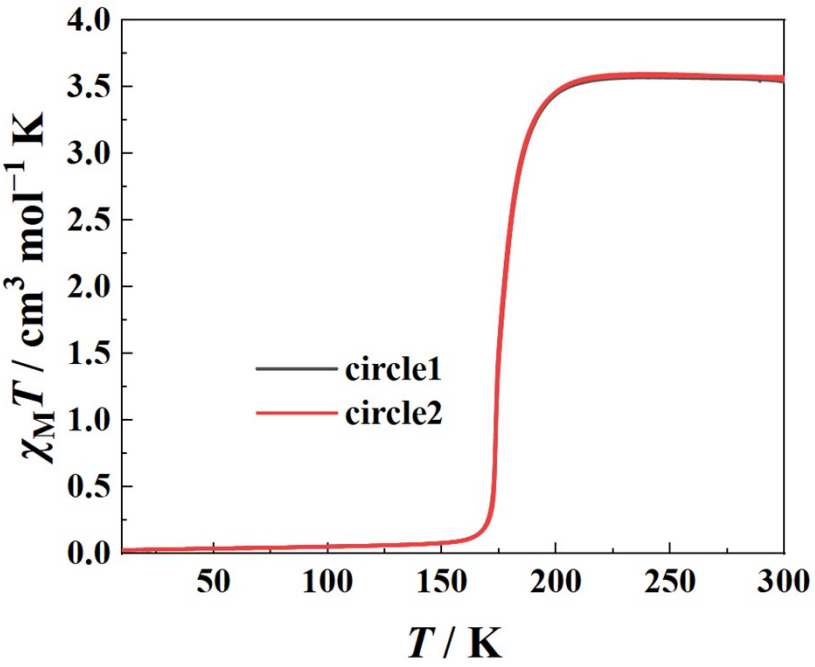

Figure S16. Variable-temperature magnetic susceptibilities of **3**.

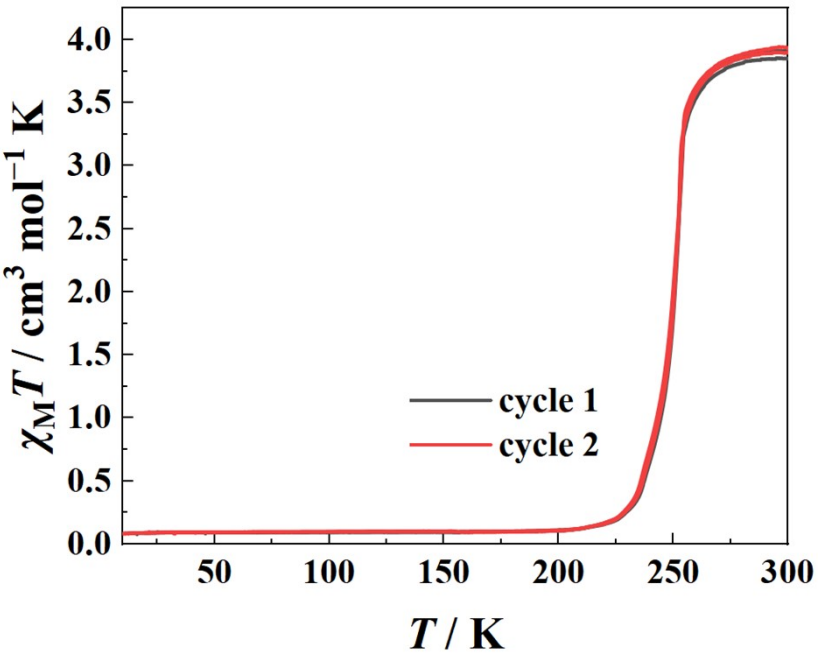

Figure S17. Variable-temperature magnetic susceptibilities of **1-SE**.

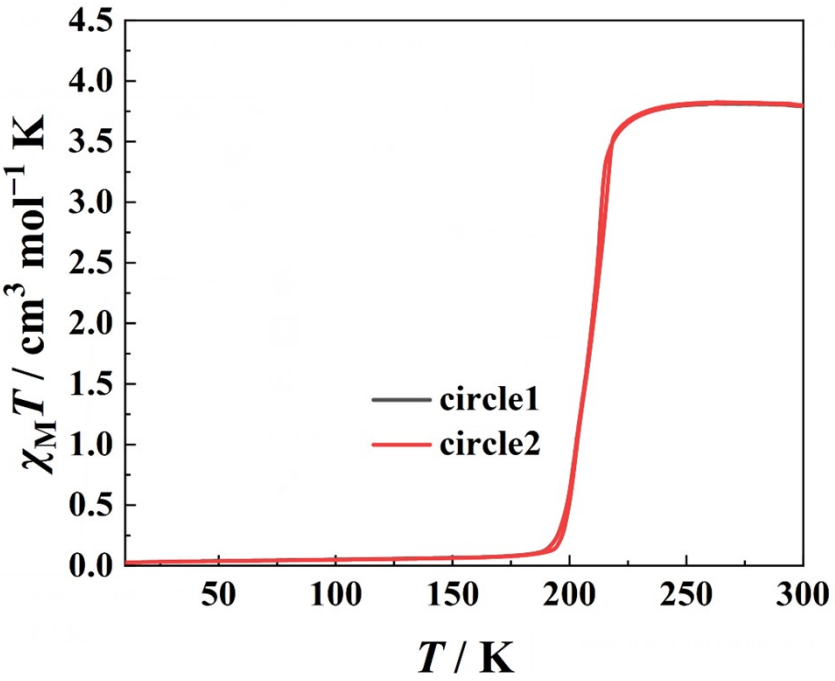

Figure S18. Variable-temperature magnetic susceptibilities of **2-SE**.

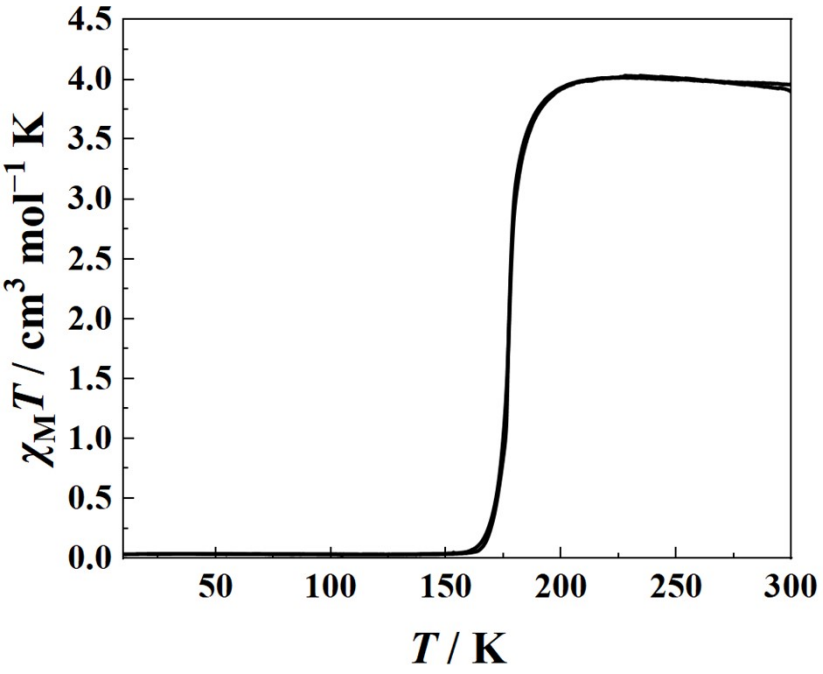

Figure S19. Variable-temperature magnetic susceptibilities of **3-SE**.

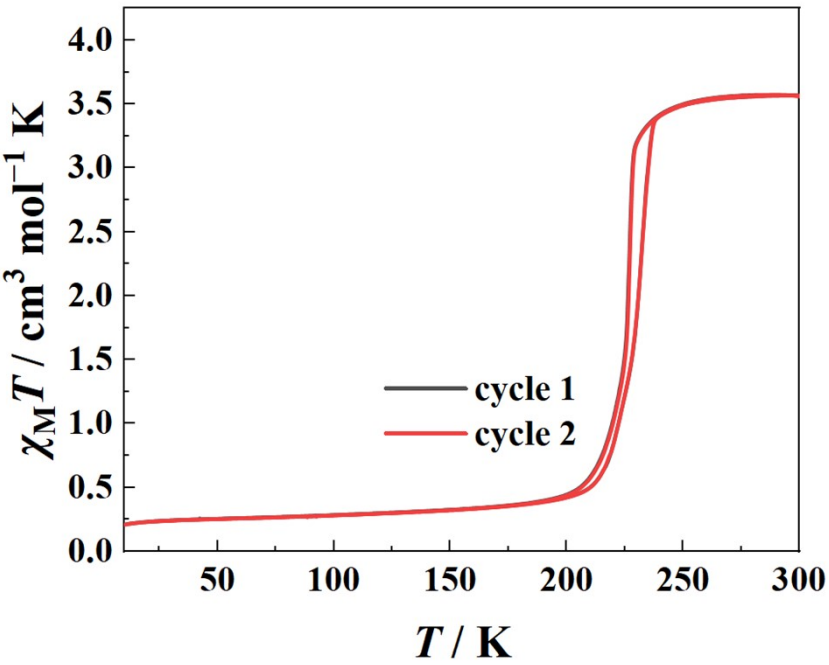

Figure S20. Variable-temperature magnetic susceptibilities of **1-dry**.

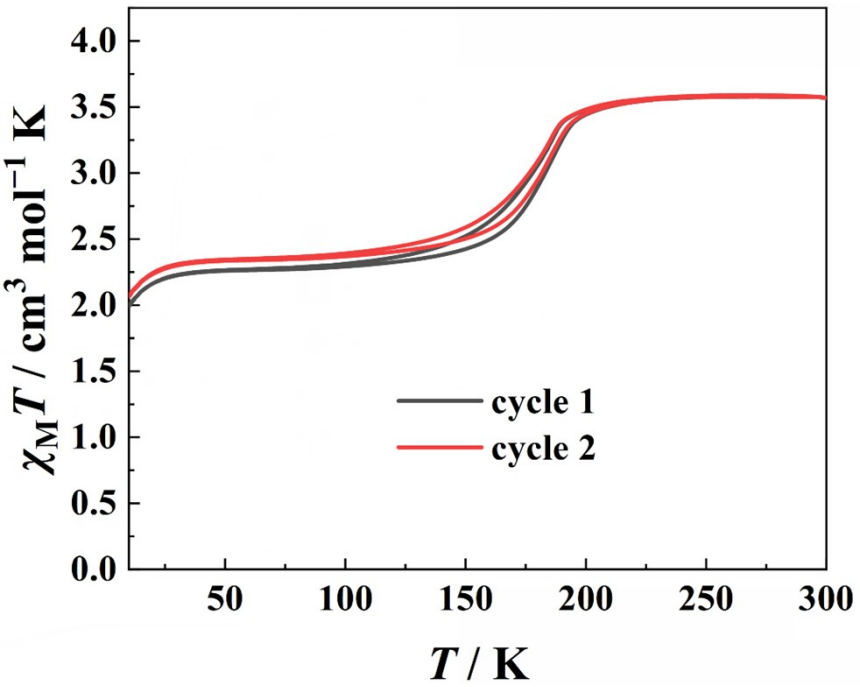

Figure S21. Variable-temperature magnetic susceptibilities of **2-dry**.

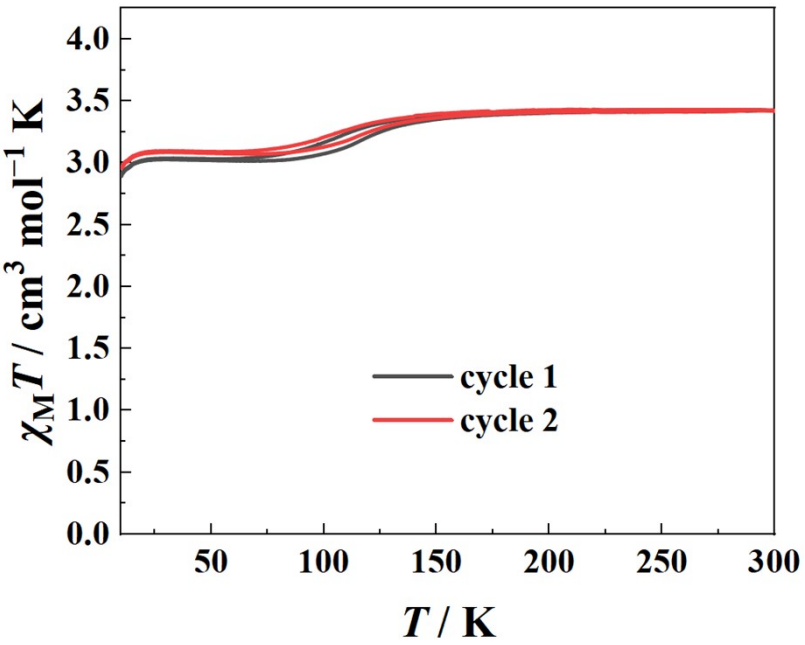

Figure S22. Variable-temperature magnetic susceptibilities of **3-dry**.

DSC

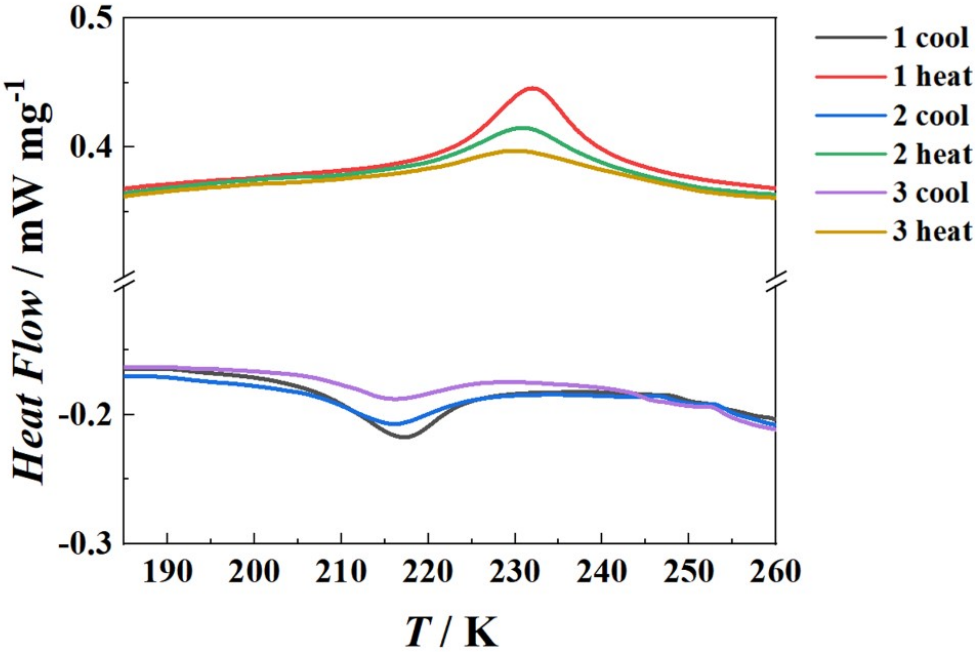

Figure S23. Differential scanning calorimetry (DSC) curves with a sweep rate of 10 K min^{-1} for **1**.

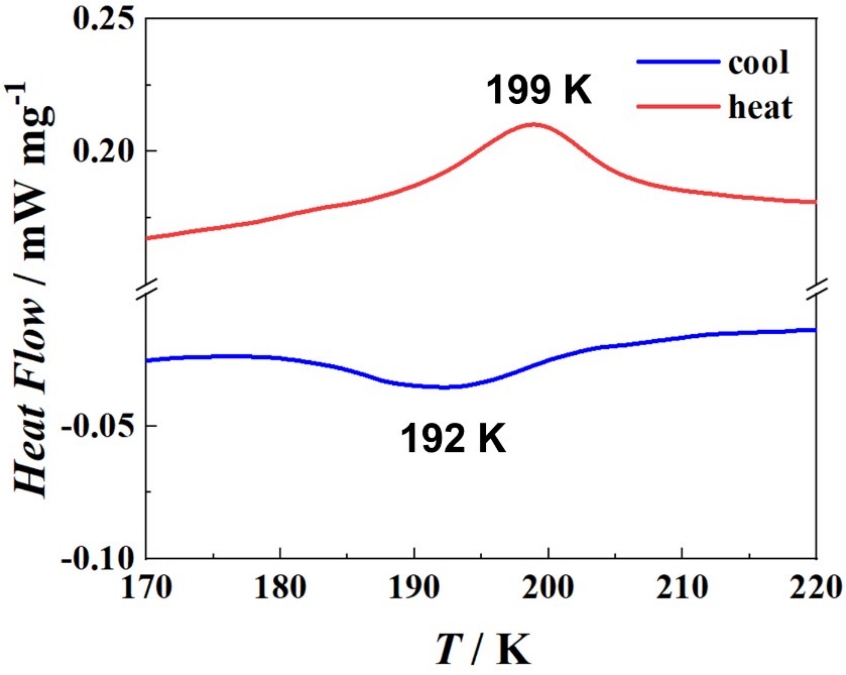

Figure S24. Differential scanning calorimetry (DSC) curves with a sweep rate of 10 K min^{-1} for **2**.

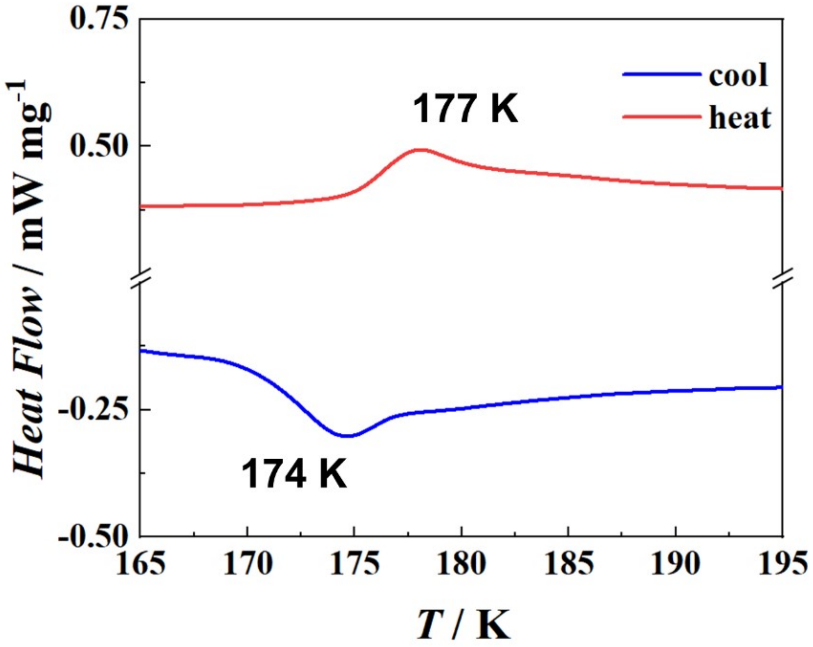

Figure S25. Differential scanning calorimetry (DSC) curves with a sweep rate of 10 K min^{-1} for **3**.

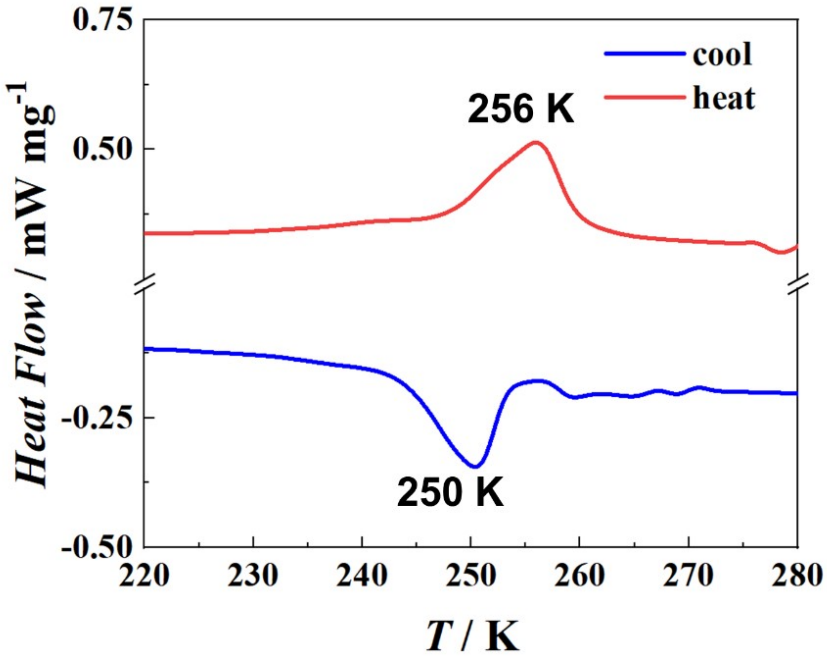

Figure S26. Differential scanning calorimetry (DSC) curves with a sweep rate of 10 K min^{-1} for **1-SE**.

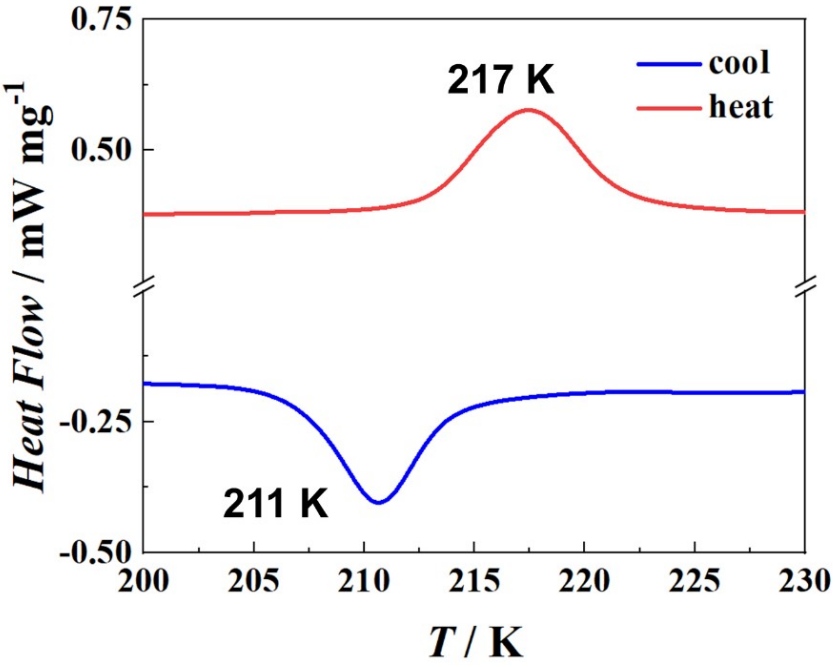

Figure S27. Differential scanning calorimetry (DSC) curves with a sweep rate of 10 K min^{-1} for **2-SE**.

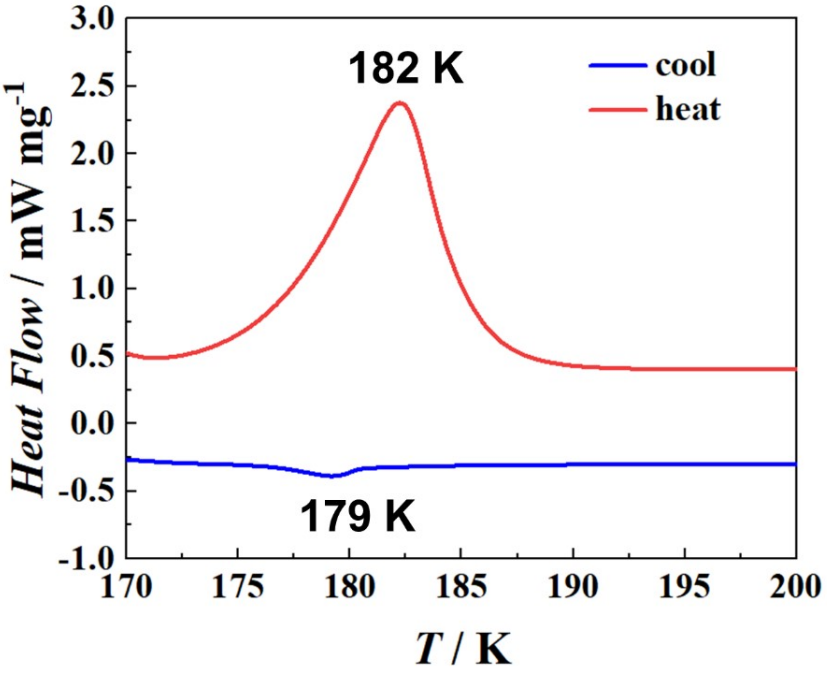

Figure S28. Differential scanning calorimetry (DSC) curves with a sweep rate of 10 K min^{-1} for **3-SE**.

IR

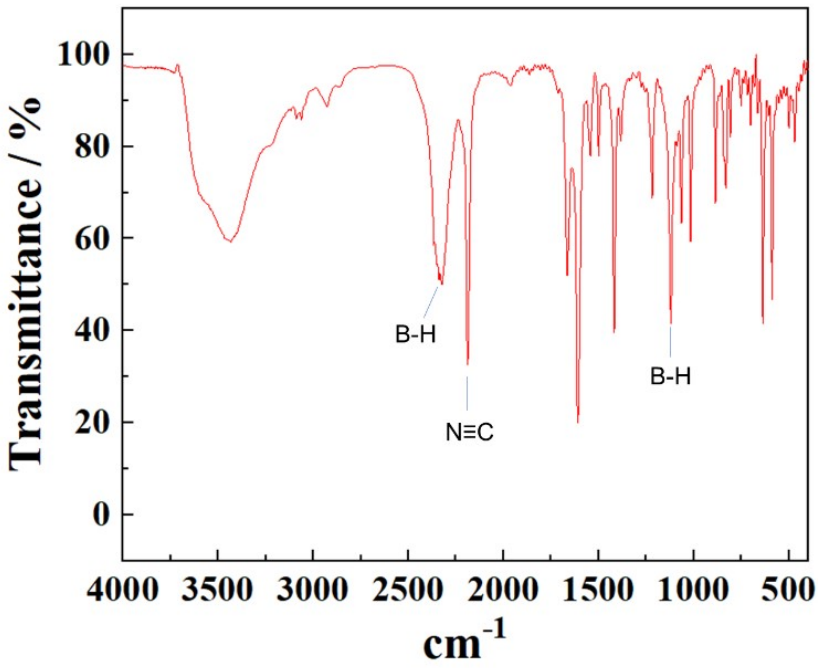

Figure S29. The infrared (IR) spectrum of **1**. B-H stretching vibration of $NCBH_3^-$ is 2324 cm^{-1} ; B-H bending vibration of $NCBH_3^-$ is 1120cm^{-1}.

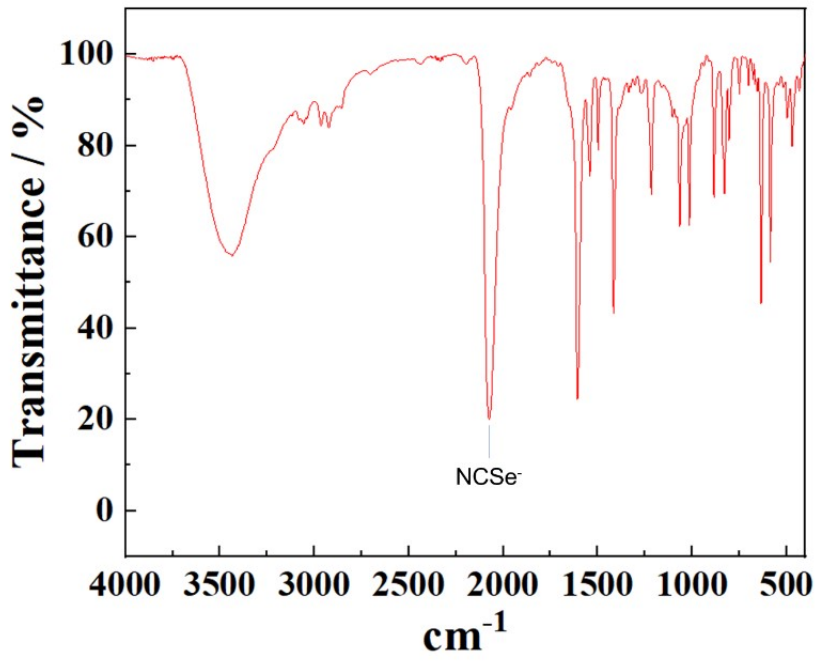

Figure S30. The infrared (IR) spectrum of **2**.

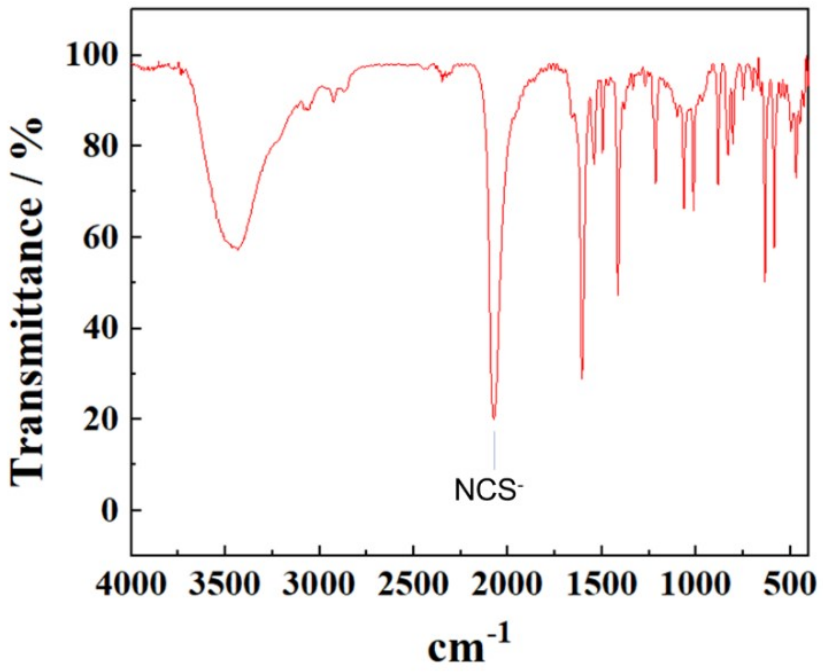

Figure S31. The infrared (IR) spectrum of **3**.

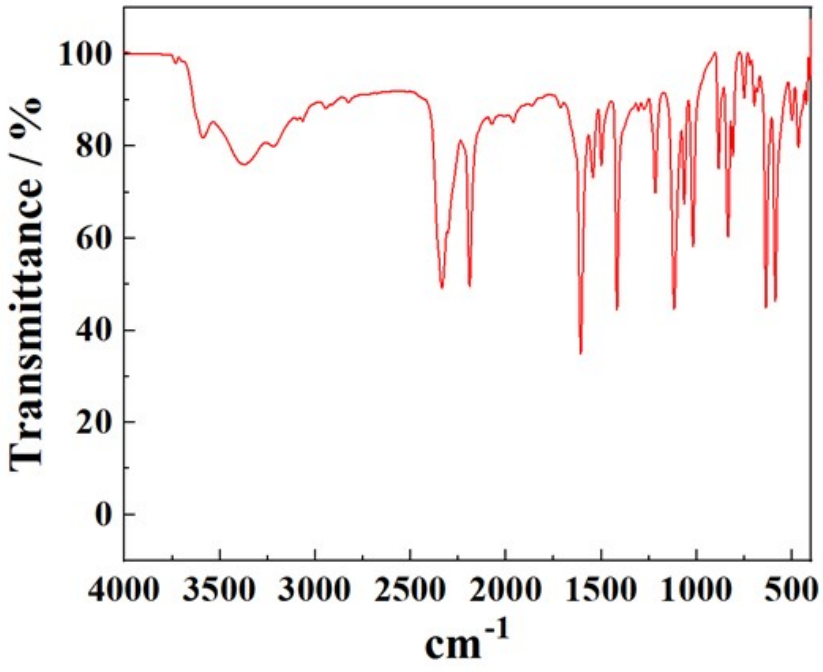

Figure S32. The infrared (IR) spectrum of **1-SE**.

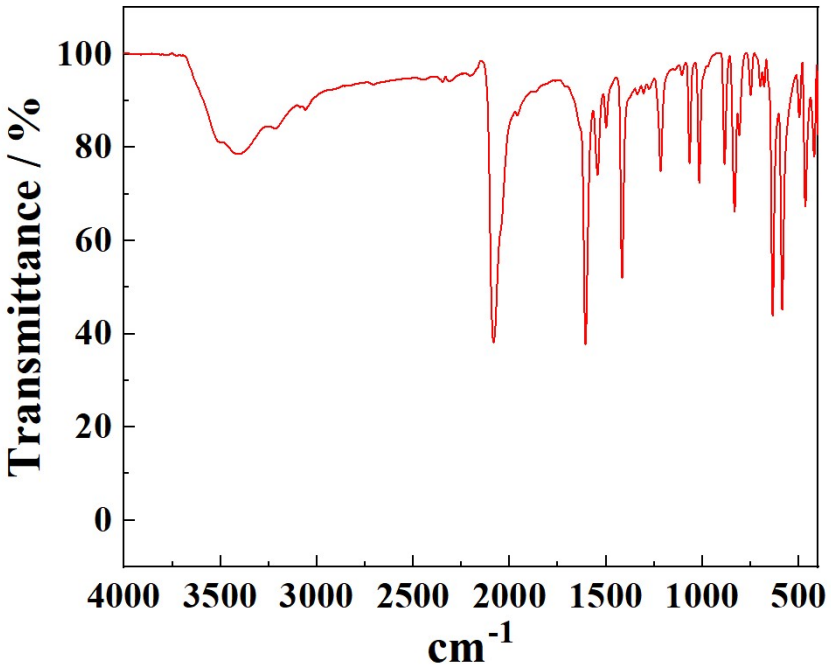

Figure S33. The infrared (IR) spectrum of **2-SE**.

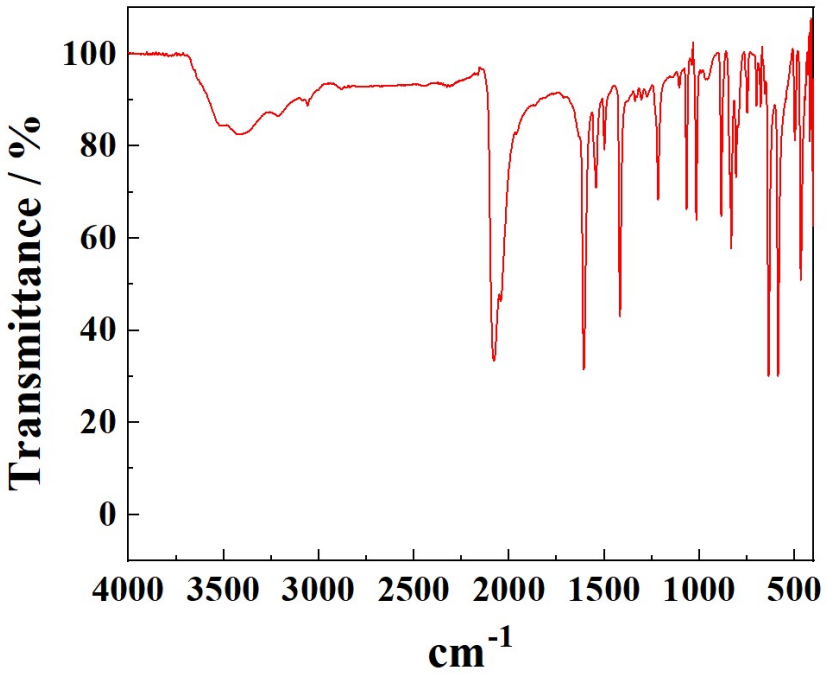

Figure S34. The infrared (IR) spectrum of **3-SE**.

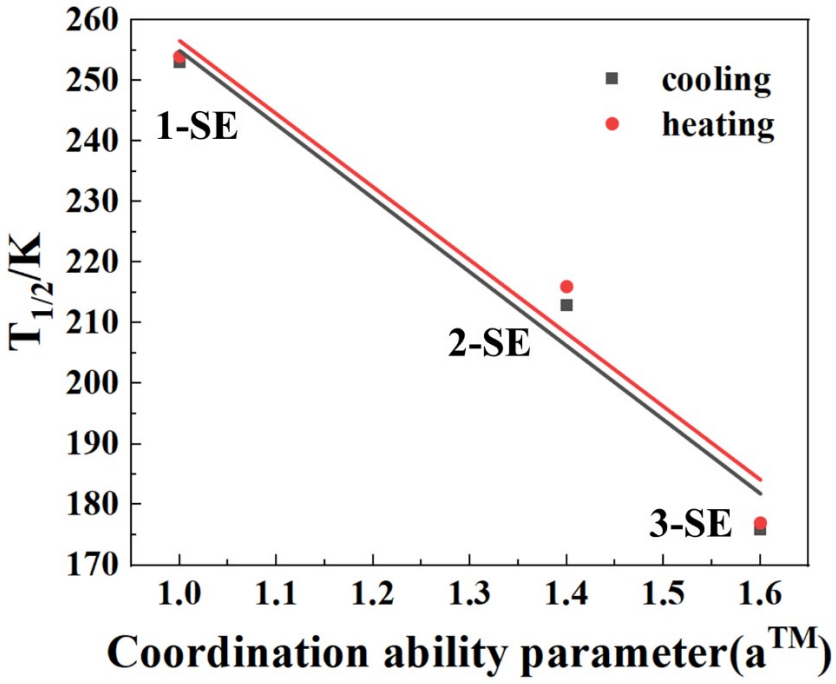

Figure S35. NCX's a^{TM} values against T_c plot of **1-SE, 2-SE** and **3-SE**. R^2 = 0.97 (black line), R^2 = 0.96 (red line).